Journal of Alloys and Compounds 882 (2021) 160686

Contents lists available at ScienceDirect

Journal of Alloys and Compounds

journal homepage: www.elsevier.com/locate/jalcom

Experimental and theoretical investigation of the mechanical characteristics of sillenite compound: $Bi_{12}GeO_{20}$

Gokhan Surucu[a,b,*], Mehmet Isik[c], Aysenur Gencer[d], Nizami Gasanly[a]

[a] Department of Physics, Middle East Technical University, 06800 Ankara, Turkey
[b] Department of Electrical and Energy, Ahi Evran University, Kirsehir 40100, Turkey
[c] Department of Electrical and Electronics Engineering, Atilim University, 06836 Ankara, Turkey
[d] Department of Physics, Karamanoglu Mehmetbey University, Karaman 70100, Turkey

ARTICLE INFO

Article history:
Received 23 March 2021
Received in revised form 16 May 2021
Accepted 1 June 2021
Available online 4 June 2021

Keywords:
$Bi_{12}GeO_{20}$
Sillenites
Density functional theory
Nanoindentation
Mechanical properties

ABSTRACT

The present study reports the mechanical and elastic characteristics of $Bi_{12}GeO_{20}$ (BGO) compound by experimental nanoindentation measurements and density functional theory (DFT) calculations. X-ray diffraction pattern of BGO was plotted and revealed diffraction peaks were associated with Miller indices of cubic crystalline structure with lattice constant of a = 10.304 Å. Two- and three-dimensional representations of Young's modulus, linear compressibility, shear modulus and Poisson's ratio were presented according to DFT calculations. The calculated elastic constants pointed out the mechanically stable and anisotropic behavior of the BGO. The hardness and Young's modulus ranges of the BGO calculated from DFT studies were found as 3.7–6.3 GPa and 61.7–98.9 GPa, respectively. Hardness and Young's modulus of BGO single crystal were also obtained by analyzing force-dependent nanoindentation experimental data. It was observed that hardness and Young's modulus decrease with increase of load in the low applied loads and then reaches saturation in the high applied loads. This behavior is known as indentation size effect. True hardness value was determined from proportional specimen resistance model as 4.1 GPa. The force independent region presented the Young's modulus as 114 GPa.

1. Introduction

$Bi_{12}GeO_{20}$ (abbreviated as BGO) belongs to the family of sillenite compounds formulated as $Bi_{12}XO_{20}$ (X: Ge, Si, Ti). The members of this group take significant attention due to their attractive characteristics utilized in photocatalytic, electro-optical, optical data processing, optical detectors, holography, nonlinear optical device and solar energy applications [1–6]. BGO have important role in these applications and also known as Faraday rotator crystal due to its large magneto-optical quality [7]. The heterostructures formed with BGO have been also investigated in recent years from the standpoint of device applications [8–10].

The basic structural, optical and electrical characteristics of BGO were reported from both theoretical and experimental studies. The BGO compound crystallizes in cubic form having lattice constant of a = 10.416 Å [11]. In its cubic structure, GeO_4 tetrahedra occupies the corners of the cube and Bi-atoms are surrounded by O-atoms in the cube center. BGO having band gap energy of ~3.2 eV belongs to the wide band gap semiconductor family. This wide band gap makes BGO a potential compound in optoelectronic devices operating at ultraviolet light. There are lots of papers reporting band gap energy of BGO around 2.6 eV [12–14]. Sillenites are known as defective compounds and reported lower band gap energy of 2.6 eV than accepted energy of 3.2 eV was associated with transition taking place between defect center and conduction/valence bands [15,16]. The analyses of spectroscopic ellipsometry data revealed the presence of four strong absorptions within the band structure at energies around 3.49, 4.11, 4.67 and 5.51 eV [12]. Relative permittivity, resonant frequency and quality factor parameters were found as 37.0, −32.8 ppm/°C and 3137 GHz, respectively [17].

Theoretical and experimental studies have been extensively focused on structural, optical and electrical characterization of BGO. However, determination of mechanical and elastic characteristics of BGO has not been given in detail to the best of our knowledge. In Ref. [18], mechanical and elastic properties of BGO were given as limited from density functional theory (DFT) studies. The aim of the present paper is to investigate mechanical and elastic properties of BGO by performing experimental nanoindentation measurements and

* Corresponding author at: Department of Physics, Middle East Technical University, 06800 Ankara, Turkey.
E-mail address: g_surucu@yahoo.com (G. Surucu).

https://doi.org/10.1016/j.jallcom.2021.160686
0925-8388/

theoretical DFT calculations. The nanoindentation experiments have not been carried out up to now and the present study gives the hardness and Young's modulus of the BGO single crystals for the first time as a result of analyses of force-dependent nanoindentation measurements. The various elastic constants and corresponding mechanical parameters (Young's modulus, bulk modulus, shear modulus, Poisson's ratio) were determined from the DFT calculations. The reported mechanical and elastic characteristics would be remarkable interest of subject in device application field of the BGO compound.

2. Calculation and experimental details

DFT calculations of the BGO compound were accomplished using the Vienna Ab-initio Simulation Package (VASP) [19]. The generalized gradient approximation (GGA) with the Perdew-Burke-Ernzerhof (PBE) [20] exchange correlation functional was considered for the electron-electron interactions. The electron and ion interactions were studied using the Projector Augmented Wave (PAW) method [21,22]. The cut-off energy for the wave functions were taken as 520 eV and the k-points were sampled as 4 × 4 × 4 with a gamma centered grid. The structural optimization for BGO was carried out until an energy convergence criterion of 10^{-11} eV per unit cell and a force convergence criterion of 10^{-10} eV/Å. The elastic parameters were calculated considering stress-strain method implemented in VASP. Also, the ionic contribution is included in the calculation of the elastic parameters. The directional-dependent elastic characteristics and sound wave velocities were revealed by ELATE software and Christoffel tool, respectively [23,24]. Nanoindentation experiments were performed on BGO single crystals grown by Czochralski method. The BGO crystal growth processes were detailed in Ref. [25]. Nanoindentation measurements were applied on BGO single crystal on which experiments were carried out on polished surfaces parallel to the (110) plane. CSM instrument nanoindentation system with a diamond Berkovich tip was used for experiments. The approach speed and load/unload rate were 2000 nm/min and 14 mN/min, respectively.

3. Results and discussions

3.1. Structural, mechanical and elastic properties from DFT calculations

The crystalline structure of the BGO was investigated by calculating the diffraction pattern which is represented in Fig. 1. BGO belongs to the *I*23 space group and its crystal structure was reported as cubic. The lattice constant of the cubic structure was obtained as a = 10.304 Å. The Miller indices given on the peaks in the XRD pattern with the corresponding diffraction peaks were determined from DFT calculations. The calculated lattice constant and revealed Miller indices are in good agreement with reported standard XRD pattern of BGO (JCPDS No: 34-0096).

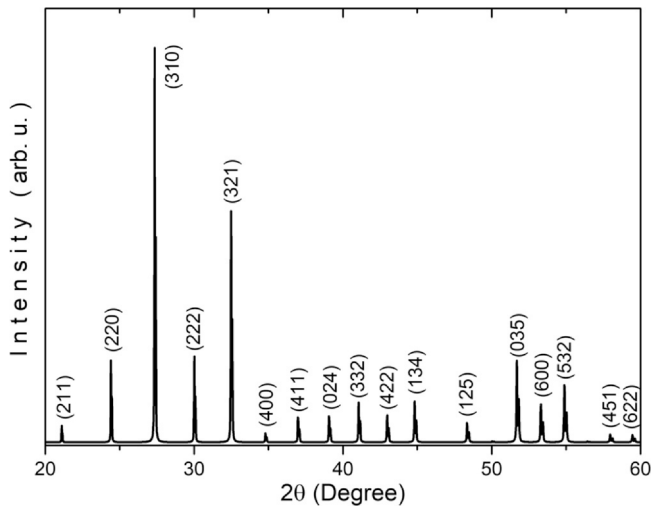

Fig. 1. XRD pattern of $Bi_{12}GeO_{20}$ from DFT calculations.

The elastic constants (C_{ij}) of BGO were calculated considering stress-strain method using VASP. The calculated elastic parameters of C_{11}, C_{12} and C_{44} related to cubic crystal structure are given in Table 1. The elastic constants may be utilized to test the mechanical stability of the BGO. For that purpose, the following Born stability criteria was considered [26].

$$C_{11} > 0, \quad C_{44} > 0, \quad C_{11} - C_{12} > 0, \quad C_{11} + 2C_{12} > 0 \tag{1}$$

The calculated elastic parameters satisfied Born stability criteria and thus BGO compound is classified as mechanically stable. In addition, the calculated elastic constants are consistent with the experimental measurements in Refs. [27,28]. However, these constants are lower than the calculated ones in Ref. [18]. These lower values are due to the consideration of the ionic contribution in the present calculations. If the elastic constants are calculated for rigid ions without ionic contribution, the determined values will be 214.15 GPa, 75.19 GPa and 63.18 GPa for C_{11}, C_{12} and C_{44}, respectively. These values are consistent with the Ref. [18]. However, the elastic constants calculated with the ionic contribution are considered due to the more consistency with the experiments in this study. The elastic parameters were also used to get mechanical characteristics of bulk modulus (B), shear modulus (G), Young's modulus (E) and Poisson's ratio (v) by applying Voight-Reuss-Hill approximation [29–31]. The calculated mechanical parameters were presented in Table 1. The higher value of Young's modulus than shear and bulk moduli indicates that BGO remarkably resists to the length change when a push or pull was applied. The Poisson's ratio is the length change in the perpendicular direction of a material when a push or pull applied and if it is around 0.1 and 0.25 for covalent and ionic bonding characteristics, respectively [32]. The calculated v = 0.26 value of BGO points out the dominantly ionic bonding characteristic of the compound. Pugh's modulus given as G/B ratio is also taken into account to get information about bonding characteristics. It was reported that G/B is around 0.6 and 1.1 for dominant ionic and covalent bonding, respectively [32]. The calculated G/B = 0.575 ratio supports the presence of dominantly ionic bonding in the compound. These listed values in Table 1 could be compared with the literature and it is found that these results are lower than Ref. [18]. These differences result from the ionic contribution in the calculation of the elastic constants. Because the elastic constants calculated for rigid ions are higher than the ones with ionic contribution. Therefore, the results in Ref. [18] is higher than the present study. $Bi_{12}SiO_{20}$ (BSO) is another attractive member of sillenite family and exhibits very similar structural, optical, electrical and mechanical characteristics with BGO. There are few papers on mechanical investigation of BSO. It would be more informative to compare reported mechanical parameters of BSO with revealed values of BGO in the present paper. The bulk modulus values were reported as 63.4 GPa from theoretical calculations [33], 63.1 GPa from ultrasonic measurements [33], 63.9 GPa from resonant ultrasound spectroscopy [34], 63.1 GPa from Brillouin spectroscopy [34] and 76.5 GPa from DFT studies [34]. As seen from the reported values, there exist a consistency around 63 GPa. The calculated bulk modulus of 51.6 GPa of BGO is considered as consistent with ~63 GPa. Fig. 2 represents the directional dependencies of Young's modulus, linear compressibility, shear modulus and Poisson's ratio in 2D and 3D. In the figure, the blue shapes and curves correspond to the maximum values of this parameter while the green ones correspond to the minimum values. As seen from the plots, linear compressibility is independent of direction (isotropic) while other parameters are

Table 1
Elastic constants (C_{ij} in GPa) and mechanical properties (Bulk modulus (B in GPa), Shear modulus (G in GPa), Young's modulus (E in GPa), Poisson's ratio (ν), G/B *ratio*, B/G ratio and hardness (H in GPa) of $Bi_{12}GeO_{20}$.

Reference	C_{11}	C_{12}	C_{44}	B	G	E	ν	G/B	B/G	H
This study	107.5	23.7	23.7	51.6	29.7	74.7	0.26	0.575	1.74	8.63
Ref. [27][a]	128.0	30.5	25.5							
Ref. [28][a]	120.0	39.0	25.0							
Ref. [18][b]	206.69	73.57	61.19	117.9	63.3	161.1	0.27		1.86	

[a] Experimental studies.
[b] DFT study.

anisotropic. The maximum values are obtained in the x, y and z directions for the Young's modulus while the ones are obtained in the 45° between the x, y and z axes for the shear modulus and Poisson's ratio. The Vickers hardness can be calculated using the expression [35].

$$H_v = 2(k^2G)^{0.585} - 3 \quad (2)$$

where $k = G/B$. According to Eq. (2), shear modulus significantly affects the hardness calculation. Since BGO exhibits anisotropic behavior, the maximum and minimum values of shear modulus given in Table 2 may be used to get the range of hardness. Under the light of Eq. (2), the hardness values were found as 3.7 and 6.3 GPa using G_{min} and G_{max}, respectively. The usage of G = 29.7 GPa reported in Table 1 gives the hardness value as 4.6 GPa which presents an average value for BGO compound.

The calculated elastic parameters are also utilized to get information about the anisotropic behavior of the BGO compound. A solid crystal exhibiting cubic symmetry has shear anisotropy factors of A and A_- for (100) and (110) directions, respectively [36]. The shear anisotropic factors are calculated using the following relations

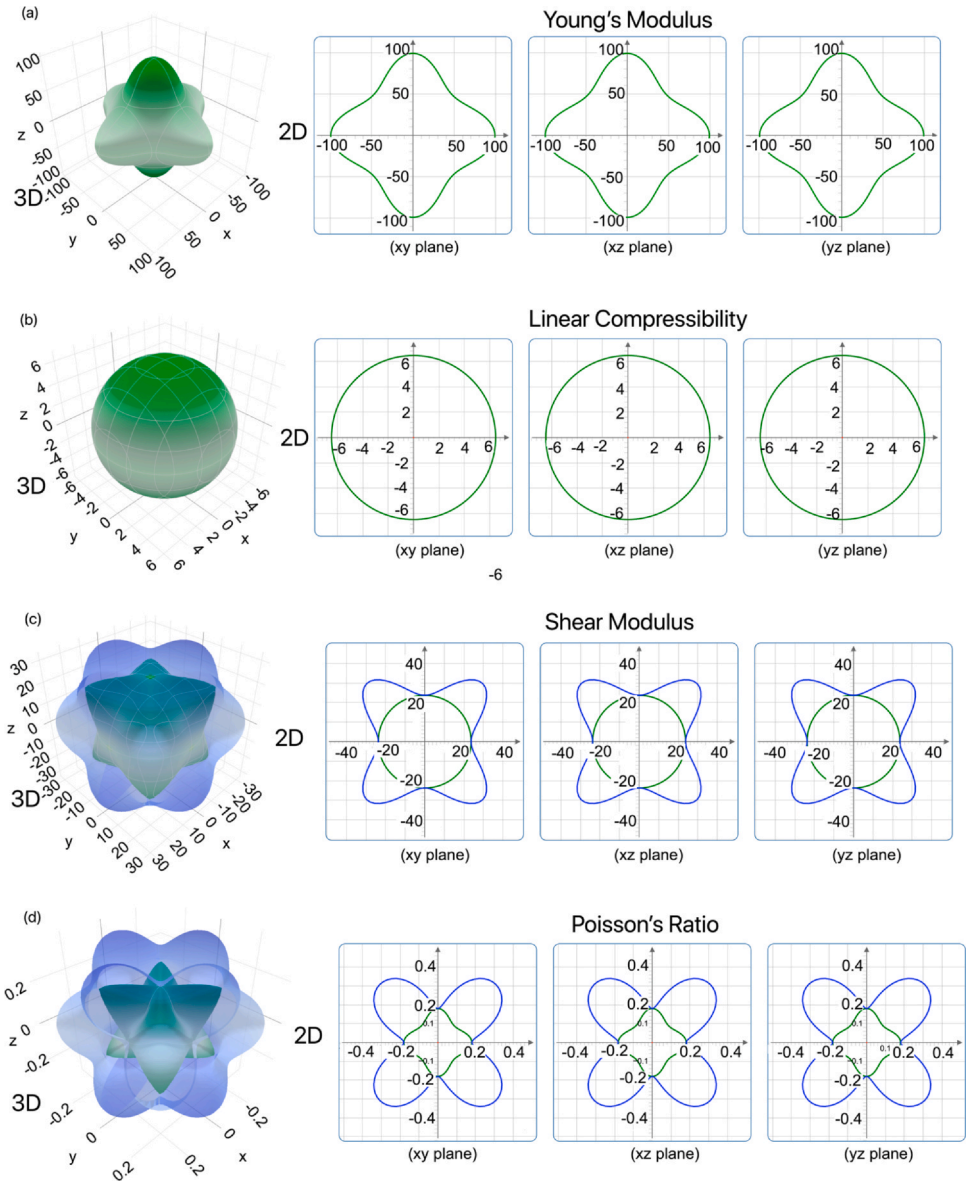

Fig. 2. Two- and three-dimensional representations of (a) Young's modulus, (b) linear compressibility, (c) shear modulus and (d) Poisson's ratio.

Table 2
Minimum and maximum values of Young's modulus (E in GPa), hardness (H in GPa), linear compressibility (β), shear modulus (G) and Poisson's ratio (ν).

	Young's modulus		Hardness		Linear compressibility		Shear modulus		Poisson's ratio	
	E_{min}	E_{max}	H_{min}	H_{max}	β_{min}	β_{max}	G_{min}	G_{max}	ν_{min}	ν_{max}
$Bi_{12}GeO_{20}$	61.7	98.9	3.7	6.3	6.46	6.46	23.7	41.9	0.12	0.44

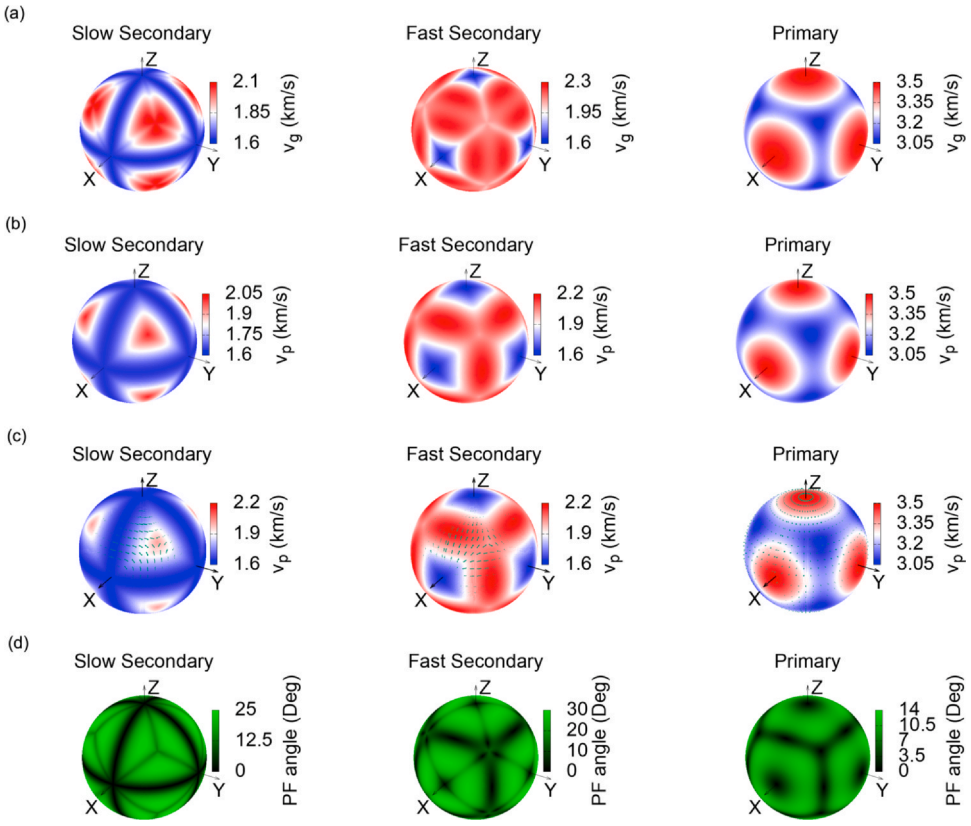

Fig. 3. (a) Group velocity, (b) phase velocity, (c) polarization of sound waves, (d) power flow angle for $Bi_{12}GeO_{20}$.

$$A = \frac{2C_{44}}{(C_{11} - C_{12})} \quad \text{and} \quad A_{-} = C_{44}(C_L + 2C_{12} + C_{11})/(C_L C_{11} - C_{12}^2) \tag{3}$$

where $C_L = C_{44} + (C_{11} + C_{12})/2$. The elastic constants of isotropic materials satisfy the $2C_{44} = (C_{11} - C_{12})$ condition and giving 1 for anisotropy factors. The anisotropy factors were obtained from these relations as 0.566 for (100) and 0.640 for (110). These calculated factors indicate the anisotropic nature of the BGO compound.

Fig. 3 shows the directional dependencies of group and phase velocities, polarization of sound waves and power flow angle of BGO in three (3D) dimensions. Transverse wave velocities (V_{TA}) are indicated by slow and fast secondary spheres while the longitudinal velocity (V_{LA}) is presented by primary sphere in the Fig. 3. The following expressions relate the wave velocities to elastic constants and mass density (ρ) [37].

$$V_{LA}[100] = (C_{11}/\rho)^{1/2}$$
$$V_{TA1}[010] = V_{TA2}[001] = (C_{44}/\rho)^{1/2}$$
$$V_{LA}[110] = ((C_{11} + C_{12};\ + 2C_{44})/2\rho)^{1/2}$$
$$V_{TA1}[1\bar{1}0] = ((C_{11} - C_{12})/\rho)^{1/2} \tag{4}$$

$$V_{LA}[111] = ((C_{11} + 2C_{12} + 4C_{44})/3\rho)^{1/2}$$
$$V_{TA1}[11\bar{2}] = V_{TA2}[11\bar{2}]((C_{11} - C_{12} + C_{44})/3\rho)^{1/2}$$

Taking into consideration the elastic parameters given in Table 1 and above-given expressions, it may be said that the longitudinal wave velocity along [100] direction is higher than the transverse wave velocities along [010] and [001] directions. Moreover, the longitudinal wave velocity along [110] and [111] directions are higher than the transverse wave velocity along [$1\bar{1}$010], [001], [$11\bar{2}$] directions. The 3D plots given in Fig. 3a point out that the group velocity gets the highest values for the primary mode in all axis. On the other hand, the slow and fast secondary modes are slow along the x, y, and z axis and take higher velocities in the other planes. The similar direction-velocity behavior was also observed for the phase velocity as indicated in Fig. 3b. The directional dependent polarization of the sound waves represented in Fig. 3c signs that the primary mode presents the pseudo-longitudinal polarization whereas the secondary mode exhibits the pseudo-transverse polarization. The directional dependent power flow angle indicated in Fig. 3d exhibits different behavior for all modes due to presence of differences in the group and phase velocities.

3.2. Mechanical properties from nanoindentation measurements

Nanoindentation is an effective experimental method used to obtain mechanical parameters of different type of compounds like single crystals, ceramics, thin films and nanostructures. The hardness and Young's modulus of the BGO single crystal were also determined by carrying out the nanoindentation experiments at

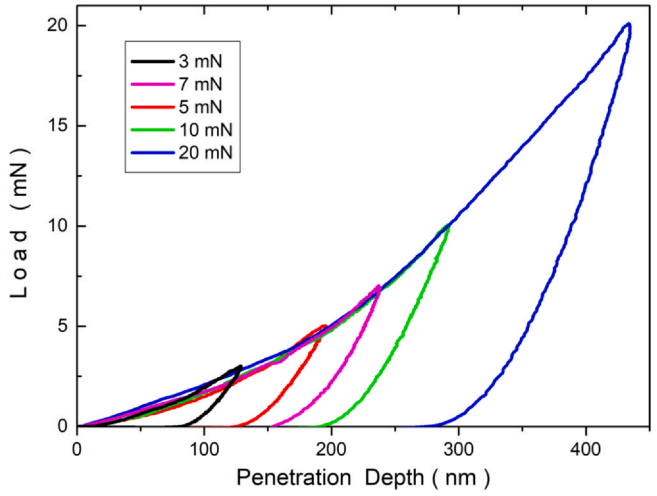

Fig. 4. Load vs. penetration depth plots for $Bi_{12}GeO_{20}$ single crystals.

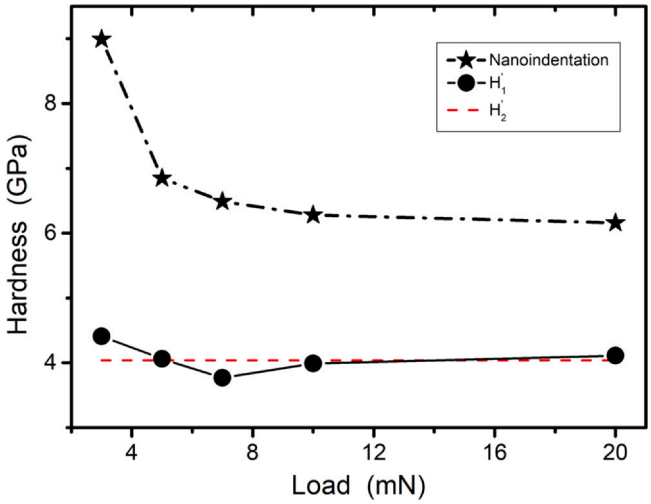

Fig. 5. Load dependencies of nanoindentation hardness (H), true hardness (H_1') and (H_2').

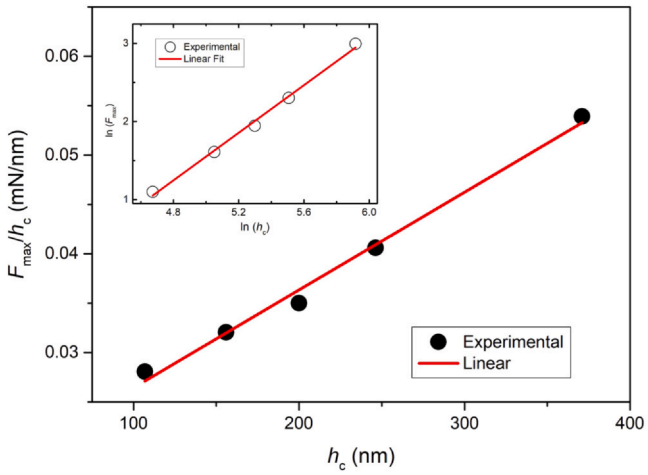

Fig. 6. The plot of ln(F_{max}) vs. ln(h_c). Inset indicates the plot of ln(F_{max}) vs. ln(h_c). Solid lines show linear fits.

different loads between 3 and 20 mN. The load was applied on the crystal surface corresponding to (001) plane. The measured load (F) vs. penetration depth (h) plots are shown in Fig. 4. Each plot exhibits loading (plastic) and unloading (elastic) regions.

Hardness (H) and Young's modulus (E) of the BGO single crystal were obtained from software equipped on the used tester experimental device. The calculations accomplished by the software are briefly given as follows: Hardness is related to indenter maximum load (F_{max}) and projected contact area (A) as [38].

$$H = \frac{F_{max}}{A} \tag{5}$$

where $A = 24.56h_c^2$ for perfect Berkovich indenter and true contact depth (h_c) is determined from the initial part of the unloading curve. The slope (dF/dh) of this portion and intersection point of the linear fitted line on the indentation depth axis are equal to stiffness (S) and h_c, respectively. Oliver-Pharr analyses present the following expressions [39].

$$S = 2\beta E_r \sqrt{\frac{A}{\pi}} \tag{6}$$

$$\frac{1}{E_r} = \frac{1-\nu_f^2}{E} + \frac{1-\nu_i^2}{E_i} \tag{7}$$

where E_r = 1141 GPa is the elastic modulus of the diamond used as tip in indenter, β = 1.034 for Berkovich indenter, Poisson's ratios ν_f and ν_i of used crystal and indenter, respectively, are ν_i = 0.07 and ν_f = 0.26. The load-dependent hardness plot is shown in Fig. 5. As seen from the figure, there exist two behaviors in the plot; remarkable load-dependent region (up to ~7 mN) and nearly load-independent region (above 7 mN). This behavior is known as indentation size effect (ISE) [40] and previously observed for different compounds like B_6O [41], SiAlON [42] and silica [43].

True hardness value of the compound may be determined from proportional specimen resistance (PSR) model which was previously applied on different compounds like Ho^{3+}:BaY_2F_8 [44], Sn [45], $AlMgB_{14}$ [46] and $LiTaO_3$ [47]. In this model, F_{max} and h_c are related as

$$\frac{F_{max}}{h_c} = \delta_1 + \delta_2 h_c \tag{8}$$

where δ_1 and δ_2 are constants which were determined from the linear fit analyses of the F_{max}/h_c vs. h_c plot shown in Fig. 6. Utilizing the slope and intersection point of the fitted line on vertical axis, these constants were found as δ_1 = 0.01653 mN/nm and $\delta_2 = 9.9 \times 10^{-5}$ mN/nm^2. In the PSR model, two hardness values are defined as [44,48].

$$H_1' = \frac{F_{max} - \delta_1 h_c}{24.5h_c^2} \tag{9}$$

$$H_2' = \frac{\delta_2}{24.5} \tag{10}$$

H_1' and H_2' represent the true hardness and load-independent hardness. Using the determined δ_1 and δ_2 constants, H_1' and H_2' values were calculated for each load and load-dependent plots of these hardness values are given in Fig. 5. As seen, these two hardness values are consistent with each other and true hardness of the BGO was determined from the applied model around 4.1 GPa. This experimentally determined hardness value is in the range of 3.7–6.3 GPa revealed from DFT calculations. The ISE behavior is also indicated by Meyer's law expressed as [49].

$$F_{max} = Ah_c^n \tag{11}$$

where A is constant and n symbolize for Meyer's index. The load-independent hardness behavior gives the $n = 2$ while $n \leq 2$ shows the presence of ISE behavior. The n value was obtained as 1.52 from the slope of ln (F_{max}) vs. ln (h_c) plot shown in the inset of Fig. 6. This

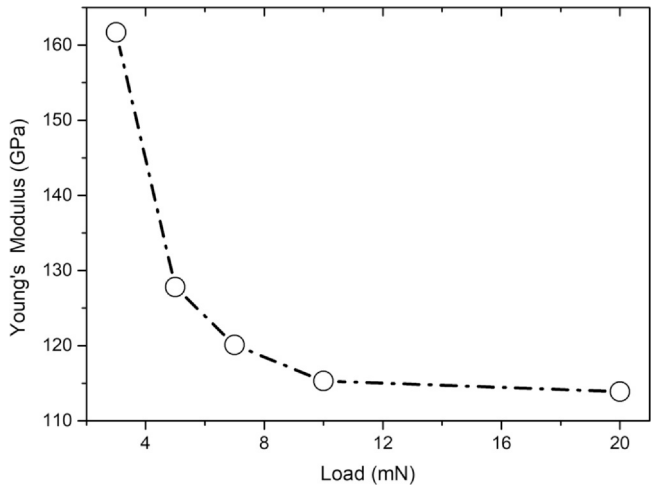

Fig. 7. Young's modulus vs. load plot for $Bi_{12}GeO_{20}$ single crystals.

value also supports the existence of ISE behavior in the BGO compound.

Young's modulus of the BGO single crystals was found under the light of Eq. (6). Fig. 7 shows the load-dependent Young's modulus plot. The plot exhibits remarkable decrease of Young's modulus with load at low loads and then reaches saturation. The load-independent Young's modulus is determined from this saturation region as 114 GPa. When experimentally determined indentation modulus was compared with calculated range of 61.7–98.9 GPa presented in Table 1, it is seen that indentation modulus is out of calculated range. The similar remarkable difference between calculated and experimentally obtained values was also reported in many papers like Refs. [35,50,51]. This difference was associated with several factors. Some of these factors are given as follows: (i) BGO is defective compound, but DFT calculations were accomplished for perfect crystalline structure. (ii) BGO compound may present grain boundaries which affect the experimental nanoindentation measurements. The grain boundaries are ignored in DFT calculations. (iii) The anisotropic behavior of BGO may lead to significant differences between calculated and experimentally determined values. (iv) The over-binding problems, binding energy and bond length differences used in theoretical calculations and utilized in nanoindentation experiments may affect the results of associated analyses.

4. Conclusion

The mechanical and elastic properties of $Bi_{12}GeO_{20}$ compound were investigated using density functional theory (DFT) calculations and experimental nanoindentation measurements. DFT calculations presented the XRD pattern of the BGO crystallizing in cubic structure with lattice constant of a = 10.304 Å. The elastic constants of the BGO were found as C_{11} = 107.5 GPa, C_{12} = 23.7 GPa and C_{44} = 23.7 GPa. BGO compound was classified as mechanically stable since calculated elastic constants satisfied Born stability criteria. The mechanical characteristics of bulk modulus (B = 51.6 GPa), shear modulus (G = 29.7 GPa), Young's modulus (E = 74.7 GPa), hardness (H = 4.6 GPa) and Poisson's ratio (v = 0.26) were calculated considering the elastic constants. The hardness and Young's modulus ranges of the BGO were calculated as 3.7–6.3 GPa and 61.7–98.9 GPa, respectively. The directional dependencies of group and phase velocities, polarization of sound waves and power flow angle of BGO in three (3D) dimensions were also presented in the present paper. The hardness and Young's modulus of BGO single crystals grown by Czochralski method were also determined by performing force-dependent nanoindentation measurements. The analyses indicated that hardness and Young's modulus decrease with increase of force in the low applied force and then reaches saturation in the high force. This force-dependent behavior of the BGO single crystal is known as indentation size effect. True hardness was found by applying proportional specimen resistance model as 4.1 GPa. The force-independent region indicated the Young's modulus as 114 GPa.

CRediT authorship contribution statement

Gokhan Surucu: Methodology, Formal analysis, Investigation, Writing - original draft. **Mehmet Isik:** Conceptualization, Data curation, Writing - original draft, Funding acquisition. **Aysenur Gencer:** Data curation, Visualization, Writing - review & editing. **Nizami Gasanly:** Supervision.

Data availability

The raw/processed data required to reproduce these findings cannot be shared at this time due to legal or ethical reasons.

Declaration of Competing Interest

The authors declare that they have no known competing financial interests or personal relationships that could have appeared to influence the work reported in this paper.

Acknowledgements

This work was supported by ATILIM University under Grant No: ATÜ-ADP-1920-03. The numerical calculations reported in this paper were performed at TUBITAK ULAKBIM, High Performance and Grid Computing Center (TRUBA resources).

References

[1] Y.T. Wu, X.J. Chang, M.L. Li, X.P. Hei, C.Q. Liu, X.M. Zhang, Studying the preparation of pure $Bi_{12}SiO_{20}$ by Pechini method with high photocatalytic performance, J. Sol Gel Sci. Technol. 97 (2021) 311–319, https://doi.org/10.1007/s10971-020-05447-0

[2] A.M. Burger, L.Y. Gao, R. Agarwal, A. Aprelev, J.E. Spanier, A.M. Rappe, V.M. Fridkin, Shift photovoltaic current and magnetically induced bulk photocurrent in piezoelectric sillenite crystals, Phys. Rev. B 102 (2020) 081113, https://doi.org/10.1103/PhysRevB.102.081113

[3] V.I. Anisimkin, E. Verona, A.S. Kuznetsova, Acoustic wave propagation along AlN on $Bi_{12}GeO_{20}$ structures, Ultrasonics 94 (2019) 314–318, https://doi.org/10.1016/j.ultras.2018.08.010

[4] X.J. Cao, L. Zhang, Y.X. Zhu, X. Zhang, C.N. Lv, C.M. Hou, Design and synthesis of sillenite-based micro/nanomaterials and their applications in photocatalysis, Prog. Chem. 32 (2020) 262–273, https://doi.org/10.7536/PC190738

[5] A.L. Moura, A.F. Pereira, A. Canabarro, J.F. Carvalho, I. de Oliveira, P.V. dos Santos, Near-infrared holographic photorefractive recording under applied electric field in undoped $Bi_{12}TiO_{20}$ sillenite crystal, Opt. Mater. 108 (2020) 110398, https://doi.org/10.1016/j.optmat.2020.110398

[6] F. Chang, X. Zhang, C. Yang, S. Peng, X. Hu, Ag nanoparticles-embellished $Bi_{12}GeO_{20}$ composites: a plasmonic system featured with reinforced visible-light photocatalytic performance and ultra-stability, Appl. Surf. Sci. 527 (2020) 146946, https://doi.org/10.1016/j.apsusc.2020.146946

[7] J.P. Slobodan, P.M. Mihailovic, Compensation of Verdet constant temperature dependence by crystal core temperature measurement, Sensors 16 (2016) 1627, https://doi.org/10.3390/s16101627

[8] C.N. Lv, L. Zhang, J.S. Hu, X.H. Huang, C.M. Hou, Band engineering of Ag-$Bi_{12}GeO_{20}$-Bi_2WO_6 composite photocatalyst: Interface regulation and enhanced photocatalytic performance, Ceram. Int. 45 (2019) 5249–5258, https://doi.org/10.1016/j.ceramint.2018.11.222

[9] X.W. Ruan, H. Hu, G.B. Che, P.J. Zhou, C.B. Liu, H.J. Dong, Fabrication of Z-scheme γ-Bi_2MoO_6/$Bi_{12}GeO_{20}$ heterostructure for visible-light-driven photocatalytic degradation of organic pollutants, Appl. Surf. Sci. 499 (2020) 143668, https://doi.org/10.1016/j.apsusc.2019.143668

[10] X.W. Ruan, H. Hu, H.N. Che, G.B. Che, C.M. Li, C.B. Liu, H.J. Dong, Facile fabrication of Ag_2O/$Bi_{12}GeO_{20}$ heterostructure with enhanced visible-light photocatalytic activity for the degradation of various antibiotics, J. Alloy. Compd. 773 (2019) 1089–1098, https://doi.org/10.1016/j.jallcom.2018.09.312

[11] M. Isik, S. Delice, N.M. Gasanly, N.H. Darvishov, V.E. Bagiev, Investigation of optical properties of $Bi_{12}GeO_{20}$ sillenite crystals by spectroscopic ellipsometry and Raman spectroscopy, Ceram. Int. 46 (2020) 12905–12910, https://doi.org/10.1016/j.ceramint.2020.02.056

[12] D. Hou, X. Hu, Y. Wen, B. Shan, P. Hu, X. Xiong, Y. Qiao, Y. Huang, Electrospun sillenite $Bi_{12}MO_{20}$ (M = Ti, Ge, Si) nanofibers: general synthesis, band structure, and photocatalytic activity, Phys. Chem. Chem. Phys. 15 (2013) 20698–20705, https://doi.org/10.1039/c3cp53945h

[13] S. Delice, M. Isik, N.M. Gasanly, N.H. Darvishov, V.E. Bagiev, Structural and temperature-tuned optical characteristics of $Bi_{12}GeO_{20}$ sillenite crystals, Chin. J. Phys. 66 (2020) 422–429, https://doi.org/10.1016/j.cjph.2020.04.005

[14] O. Pena-Rodriguez, J. Olivares, I. Banyasz, Optical properties of crystalline and ion-beam amorphized $Bi_{12}GeO_{20}$: relevance for waveguide applications, Opt. Mater. 47 (2015) 328–332, https://doi.org/10.1016/j.optmat.2015.05.050

[15] T.M. Oliveira, C. Santos, A.F. Lima, M.V. Lalic, Antisite defect as rule for photorefractive, photochromic and photocatalytic properties of $Bi_{12}MO_{20}$ (M = Ge, Si, Ti) sillenite crystals, J. Alloy. Compd. 720 (2017) 187–195, https://doi.org/10.1016/j.jallcom.2017.05.247

[16] S. Delice, M. Isik, N. Sarigul, N.M. Gasanly, Defect characterization in $Bi_{12}GeO_{20}$ single crystals by thermoluminescence, J. Lumin. 233 (2021) 117905, https://doi.org/10.1016/j.jlumin.2021.117905

[17] A. Cremades, M.T. Santos, A. Remon, J.A. Garcia, E. Dieguez, J. Piqueras, Cathodoluminescence and photoluminescence in the core region of $Bi_{12}GeO_{20}$ and $Bi_{12}SiO_{20}$ crystals, J. Appl. Phys. 79 (1996) 7186–7190, https://doi.org/10.1063/1.361434

[18] H. Koc, S. Palaz, S. Simsek, A.M. Mamedov, E. Ozbay, Elastic and optical properties of sillenites: first principle calculations, Ferroelectrics 557 (2020) 98–104, https://doi.org/10.1080/00150193.2020.1713354

[19] G. Kresse, J. Furthmüller, Efficient iterative schemes for ab initio total-energy calculations using a plane-wave basis set, Phys. Rev. B 54 (1996) 11169–11186, https://doi.org/10.1103/PhysRevB.54.11169

[20] J.P. Perdew, K. Burke, M. Ernzerhof, Generalized gradient approximation made simple, Phys. Rev. Lett. 77 (1996) 3865–3868, https://doi.org/10.1103/PhysRevLett.77.3865

[21] P.E. Blöchl, Projector augmented-wave method, Phys. Rev. B 50 (1994) 17953–17979, https://doi.org/10.1103/PhysRevB.50.17953

[22] G. Kresse, D. Joubert, From ultrasoft pseudopotentials to the projector augmented-wave method, Phys. Rev. B 59 (1999) 1758–1775, https://doi.org/10.1103/PhysRevB.59.1758

[23] R. Galliac, P. Pullumbi, F.-X. Coudert, ELATE: an open-source online application for analysis and visualization of elastic tensors, J. Phys. Condens. Matter 28 (2016) 275201, https://doi.org/10.1088/0953-8984/28/27/275201

[24] F.I. Fedorov, F.I. Fedorov, General Equations of the Theory of Elasticity, Springer, US, 1968.

[25] M. Isik, S. Delice, N.M. Gasanly, N.H. Darvishov, V.E. Bagiev, Investigation of optical properties of $Bi_{12}GeO_{20}$ sillenite crystals by spectroscopic ellipsometry and Raman spectroscopy, Ceram. Int. 46 (2020) 12905–12910, https://doi.org/10.1016/j.ceramint.2020.02.056

[26] M. Born, On the stability of crystal lattices. I, Math. Proc. Camb. Philos. Soc. 36 (1940) 160–172, https://doi.org/10.1017/S0305004100017138

[27] A.J. Slobodnik, J.C. Sethares, Elastic, piezoelectric, and dielectric constants of $Bi_{12}GeO_{20}$, J. Appl. Phys. 43 (1) (1972) 247–248, https://doi.org/10.1063/1.1660823

[28] E.A. Kraut, B.R. Tittmann, L.J. Graham, T.C. Lim, Acoustic surface waves on metallized and unmetallized $Bi_{12}GeO_{20}$, Appl. Phys. Lett. 17 (7) (1970) 271–272, https://doi.org/10.1063/1.1653397

[29] W. Voigt, Lehrbuch der Kristallphysik, B.G.Teubner, Leipzig, Berlin, 1928.

[30] A. Reuss, Berechnung der Fliessgrenze von Mischkristallen auf Grund der Plastizitatsbedingung fur Einkristalle, J. Appl. Math. Mech. 9 (1929) 49–58, https://doi.org/10.1002/zamm.19290090104

[31] R. Hill, The elastic behaviour of a crystalline aggregate, Proc. Phys. Soc. A 65 (1952) 349–354, https://doi.org/10.1088/0370-1298/65/5/307

[32] G. Surucu, M. Isik, A. Candan, X.T. Wang, H.H. Gullu, Investigation of structural, electronic, magnetic and lattice dynamical properties for XCoBi (X: Ti, Zr, Hf) Half-Heusler compounds, Phys. B Condens. Matter 587 (2020) 412146, https://doi.org/10.1016/j.physb.2020.412146

[33] L. Wiehl, A. Friedrich, E. Haussühl, W. Morgenroth, A. Grzechnik, K. Friese, B. Winkler, K. Refson, V. Milman, Structural compression and vibrational properties of $Bi_{12}SiO_{20}$ sillenite from experiment and theory, J. Phys. Condens. Matter 22 (2010) 505401, https://doi.org/10.1088/0953-8984/22/50/505401

[34] E. Haussühl, H.J. Reichmann, J. Schreuer, A. Friedrich, C. Hirschle, L. Bayarjargal, B. Winkler, I. Alencar, L. Wieh, S. Ganschow, Elastic properties of single crystal $Bi_{12}SiO_{20}$ as a function of pressure and temperature and acoustic attenuation effects in $Bi_{12}MO_{20}$ (M = Si, Ge and Ti), Mater. Res. Express 7 (2020) 025701, https://doi.org/10.1088/2053-1591/ab6ad6

[35] Q. Chen, F. Gao, T. Csanadi, J. Xu, M. Fu, M. Wang, J. Dusza, Investigation of anisotropic mechanical properties of textured $KSr_2Nb_5O_{15}$ ceramics via ab-initio calculation and nanoindentation, J. Am. Ceram. Soc. 101 (2018) 5138–5150, https://doi.org/10.1111/jace.15733

[36] K. Lau, A.K. McCurdy, Elastic anisotropy factors for orthorhombic, tetragonal, and hexagonal crystals, Phys. Rev. B 58 (1998) 8980–8984, https://doi.org/10.1103/PhysRevB.58.8980

[37] W. Bao, D. Liu, P. Li, Y. Duan, Elastic anisotropies and thermal properties of cubic TMIr (TM = Sc, Y,Lu, Ti, Zr and Hf): A DFT calculation, Mater. Res. Express 6 (2019) 086574, https://doi.org/10.1088/2053-1591/ab1f01

[38] X.D. Li, B. Bhushan, A review of nanoindentation continuous stiffness measurement technique and its applications, Mater. Charact. 48 (2002) 11–36, https://doi.org/10.1016/S1044-5803(02)00192-4

[39] W.C. Oliver, G.M. Pharr, An improved technique for determining hardness and elastic modulus using load and displacement sensing indentation experiments, J. Mater. Res. 7 (1992) 1564–1583, https://doi.org/10.1557/JMR.1992.1564

[40] W.D. Nix, H.J. Gao, Indentation size effects in crystalline materials: a law for strain gradient plasticity, J. Mech. Phys. Solids 46 (1998) 411–425, https://doi.org/10.1016/S0022-5096(97)00086-0

[41] R. Machaka, T.E. Derry, I. Sigalas, M. Herrmann, Analysis of indentation size effect in the microhardness measurements in B_6O, Adv. Mater. Sci. Eng. (2011) 539252, https://doi.org/10.1155/2011/539252

[42] E.R. Shanholtz, J.C. LaSalvia, Investigation of the indentation-size effect (iSE) in a commercial SiAlON: multifractal scaling analysis and underlying mechanisms, J. Am. Ceram. Soc. 96 (2013) 2607–2614, https://doi.org/10.1111/jace.12450

[43] M. Kazembeykia, M. Bauchyb, C.G. Hoovera, New insights into the indentation size effect in silicate glasses, J. Non Cryst. Solids 521 (2019) 119494, https://doi.org/10.1016/j.jnoncrysol.2019.119494

[44] W. Zhang, H.Z. Song, Z. Zhang, H. Luo, Y. Jiang, X. Xie, C. Yao, L. Yuan, J. Deng, W. Hu, Q. Chen, H. Huang, Q. Dai, X. Hao, Q. Liu, Determination of mechanical behaviors of Ho^{3+}:BaY_2F_8 single crystals by nanoindentation, Ceram. Int. 45 (2019) 21751–21758, https://doi.org/10.1016/j.ceramint.2019.07.176

[45] O. Sahin, O. Uzun, U. Kolemen, N. Ucar, Analysis of ISE in dynamic hardness measurements of β-Sn single crystals using a depth-sensing indentation technique, Mater. Charact. 59 (2008) 729–736, https://doi.org/10.1016/j.matchar.2007.06.005

[46] A.M. Grishin, Hardness, Young's modulus and elastic recovery in magnetron sputtered amorphous AlMgB14 films, Crystals 10 (2020) 823, https://doi.org/10.3390/cryst10090823

[47] Y. Ma, X.W. Huang, W. Hang, M. Liu, Y.X. Song, J.L. Yuan, T.H. Zhang, Nanoindentation size effect on stochastic behavior of incipient plasticity in a $LiTaO_3$ single crystal, Eng. Fract. Mech. 226 (2020) 106877, https://doi.org/10.1016/j.engfracmech.2020.106877

[48] H.S. Guder, E. Sahin, O. Sahin, H. Gocmez, C. Duran, H.A. Cetinkaya, Vickers and Knoop indentation microhardness study of β-SiAlON ceramic, Acta Phys. Polon. A 120 (2011) 1026–1033, https://doi.org/10.12693/APHYSPOLA.120.1026

[49] J. Gong, H. Miao, Z. Peng, L. Qi, Effect of peak load on the determination of hardness and Young's modulus of hot-pressed Si_3N_4 by nanoindentation, Mater. Sci. Eng. B 354 (2003) 140–145, https://doi.org/10.1016/S0921-5093(02)00940-1

[50] S.M. Aouadi, Structural and mechanical properties of TaZrN films: experimental and ab initio studies, J. Appl. Phys. 99 (2006) 053507, https://doi.org/10.1063/1.2178394

[51] C. Lamuta, D. Campi, A. Cupolillo, Z.S. Aliev, M.B. Babanly, E.V. Chulkov, A. Politano, L. Pagnotta, Mechanical properties of Si_2Te_3 topological insulator investigated by density functional theory and nanoindentation, Scr. Mater. 121 (2016) 50–55, https://doi.org/10.1016/j.scriptamat.2016.04.036